

***Final Draft***  
**of the original manuscript:**

Chen, Y.H.; Rogstroem, L.; Ostach, D.; Ghafoor, N.; Johansson-Joesaar, M.P.;  
Schell, N.; Birch, J.; Oden, M.:

**Effects of decomposition route and microstructure on  
h-AlN formation rate in TiCrAlN alloys**

In: Journal of Alloys and Compounds (2016) Elsevier

DOI: 10.1016/j.jallcom.2016.08.299

# Effects of decomposition route and microstructure on h-AlN formation rate in TiCrAlN alloys

Y.H. Chen<sup>1\*</sup>, L. Rogström<sup>1</sup>, D. Ostach<sup>2</sup>, N. Ghafoor<sup>1</sup>, M. P. Johansson-Jöesaar<sup>1,3</sup>, N. Schell<sup>2</sup>, J. Birch<sup>4</sup> and M. Odén<sup>1</sup>

<sup>1</sup> Nanostructured Materials, Department of Physics, Chemistry and Biology (IFM), Linköping University, SE-581 83 Linköping, Sweden

<sup>2</sup> Helmholtz-Zentrum Geesthacht (HZG), Max-Planck-Str. 1, D-21502 Geesthacht, Germany

<sup>3</sup> R&D Material and Technology Development, SECO Tools AB, SE-737 82 Fagersta, Sweden

<sup>4</sup> Thin Film Physics, Department of Physics, Chemistry and Biology (IFM), Linköping University, SE-581 83 Linköping, Sweden

\* Corresponding author: yuhch@ifm.liu.se

## Abstract

The phase evolution of cubic (c), solid solution  $Ti_xCr_{1-0.37x}Al_{1-0.37-x}N$  alloys with  $x=0.03$  and  $0.16$ , and the kinetics of the hexagonal (h)-AlN formation are studied via *in situ* wide angle x-ray scattering experiments during high temperature (1000-1150 °C) annealing. Spinodal decomposition was observed in  $Ti_{0.16}Cr_{0.36}Al_{0.48}N$  while  $Ti_{0.03}Cr_{0.38}Al_{0.59}N$  decomposes through nucleation and growth of h-AlN, c-TiN and c-CrAlN. h-AlN is formed from c-CrAlN domains in both cases and the formation rate of h-AlN depends on the stability of the c-CrAlN domains. In  $Ti_{0.16}Cr_{0.36}Al_{0.48}N$ , the c-CrAlN domains are stabilized by crystallographic coherency with the surrounding c-TiCrN in a microstructure originating from spinodal decomposition. This results in lower formation rates of h-AlN for this composition. These differences are reflected in higher activation energy for h-AlN formation in  $Ti_{0.16}Cr_{0.36}Al_{0.48}N$  compared to  $Ti_{0.03}Cr_{0.38}Al_{0.59}N$ . It also points out different stabilities of the intermediate phase c-CrAlN during phase decomposition of TiCrAlN alloys. Additional contributions to the low

activation energy for formation of h-AlN in  $\text{Ti}_{0.03}\text{Cr}_{0.38}\text{Al}_{0.59}\text{N}$  stems from precipitation at grain boundaries.

## 1. Introduction

Wear resistant coatings are used to improve the properties of hard metal cutting tool inserts. Among a wide range of transition metal nitrides, cubic c- $\text{Ti}_{1-x}\text{Al}_x\text{N}$  coatings are extensively used in this product segment triggered by its superior mechanical properties [1]. The high hardness after exposing the coating to high temperatures is related to spinodal decomposition [2, 3] resulting in c-TiN and c-AlN rich domains where the variations in elastic properties and the strain between domains gives rise to age hardening. However, the subsequent transformation of c-AlN to hexagonal (h)-AlN following the spinodal decomposition [3] degrades the mechanical properties of the alloy due to loss of coherency between c-TiN and c-AlN domains [4, 5].

For high-speed cutting tools the temperatures may reach above 1000 °C at the cutting zone [6]. Coating materials with improved thermal stability are needed in order for the tool to survive extended time periods or even higher temperatures. Enhanced thermal stability, in terms of suppressing the h-AlN formation during decomposition, has been demonstrated by multilayering TiAlN [7, 8] or alloying metal elements ( $M_e$ ) in  $\text{Ti}M_e\text{AlN}$  [9-12]. Specifically, the addition of Cr in TiCrAlN-alloys has shown to yield superior mechanical properties after high temperature annealing and wear resistance compared to TiAlN [13-15]. Despite a less pronounced age hardening in TiCrAlN because of lower coherency strains between Ti- and Al-rich domains when introducing Cr [7, 16], the detrimental effect on the mechanical properties by h-AlN formation is also less severe due to formation of semi-coherent interfaces between h-AlN and c-TiCrN domains [8, 16-18]. Nevertheless, the formation of h-AlN still limits the high temperature properties and the details regarding its transformation are lacking. There is a critical domain size for when the interfaces relax from semi-coherent to incoherent

during formation of h-AlN, which is Cr-content dependent [16]. In order to further improve the design of these coatings, a better understanding of the formation mechanisms of h-AlN is needed.

The decomposition path of TiCrAlN is known to be dependent on its chemical composition. In particular, spinodal decomposition is shown to be promoted with increasing Ti-content for a fixed Al-content [17]. In the case of TiAlN (no Cr), it is well known that the spinodal decomposition generates different microstructures depending on Al-content; that both the coarsening rate of the cubic domains and the subsequent c-AlN to h-AlN transformation rate depend on alloy composition [19]. In addition, the h-AlN formation rate is affected by the microstructure generated during spinodal decomposition [20]. Given that the presence of Cr causes less coherency strain and allows for formation of h-AlN with semi-coherent interfaces with TiCrN [21], our hypothesis is that the activation energy and formation rates of h-AlN are affected by the alloy composition and thus provides a tool to reveal its formation mechanism.

In this study, the phase evolution of TiCrAlN and the kinetics of h-AlN formation are investigated by *in situ* wide angle x-ray scattering (WAXS) measurements during high temperature annealing. Two TiCrAlN alloys with different Ti/Al ratios were studied to investigate the effect of the decomposition route on the kinetics of h-AlN formation. The transformation rate and activation energy of h-AlN formation differ depending on alloy composition. The kinetics of the phase transformation is discussed in terms of decomposition mechanisms and microstructural differences.

## **2. Experimental details**

The deposition of TiCrAlN coatings was performed by cathodic arc evaporation in a Sulzer Metaplas MZR323 system on both iron (Fe) foils (Goodfellow Cambridge Ltd FE000400) and cemented carbide (WC-Co) 12 wt% Co substrates (ISO geometry SNUN 120408). An application of these coatings is cutting tools, which is why WC-Co substrates were used for the *ex situ* experiments. Coatings deposited on Fe-foils were intended for *in situ* analyses where the substrate had to be removed. The deposition was carried out in 4.5 Pa N<sub>2</sub>-atmosphere, with a substrate temperature of 550 °C, and a substrate bias of -35 V. Prior to deposition, the substrates were cleaned by Ar ion etching. Compound cathodes of TiAl and CrAl with different Ti/Al and Cr/Al ratios are used in each deposition (first deposition: Ti<sub>33</sub>Al<sub>67</sub>-Cr<sub>50</sub>Al<sub>50</sub>-Ti<sub>75</sub>Al<sub>25</sub>; second deposition: Cr<sub>50</sub>Al<sub>50</sub>-Ti<sub>45</sub>Al<sub>55</sub>-Cr<sub>30</sub>Al<sub>70</sub>) for obtaining various compositions of TiCrAlN coatings, as shown in **Figure 1(a)**. To prevent chemical reactions between coating and substrate materials during *in situ* annealing experiments (~1100 °C), powder samples were prepared following deposition by dissolving the iron substrates in hydrochloric acid, a procedure that completely removes the Fe while the structure of the coating is retained [7]. The obtained coating flakes were cleaned in deionized water and ground to a fine powder. The metal content of the coating powder was measured by energy-dispersive x-ray spectroscopy (EDS) in a Leo 1550 Gemini scanning electron microscope operated at 20 kV. Based on their similar Cr-content and different Ti/Al-ratio, two powder compositions were selected for *in situ* characterization: Ti<sub>0.16</sub>Cr<sub>0.36</sub>Al<sub>0.48</sub>N and Ti<sub>0.03</sub>Cr<sub>0.38</sub>Al<sub>0.59</sub>N.

The *in situ* x-ray scattering experiments were performed at the beamline P07 (high-energy materials science beam line) at PETRA III, DESY in Hamburg using an 80 keV x-ray beam with a size defined to 500 × 500 μm<sup>2</sup> using slits. Isothermal anneals were carried out in a vacuum chamber at a working pressure of 1.6 mPa for 3-5 hours and isothermal annealing temperatures (T<sub>max</sub>) were between 1000 °C and 1150 °C with a heating and cooling rate of 20 K min<sup>-1</sup>. The experimental setup is schematically shown in **Figure 1(b)**. The powder was

placed on an open ceramic cylinder holder inside a Boralectric heating tube (a graphite heater coated with boron nitride). Three annealing experiments with different  $T_{\max}$  were carried out for each TiCrAlN coating. The temperature was controlled by an Eurotherm controller connected to a thermocouple placed close to the powder position. The precise annealing temperature was calibrated in advance by measuring the temperature of a Si wafer placed at the sample position using a two-color CellaTemp pyrometer. The x-ray beam was let through the vacuum chamber by x-ray transparent viewports, and the diffracted x-rays were recorded with a two-dimensional area detector (Perkin Elmer) with a pixel size of 200 by 200  $\mu\text{m}^2$ . The detector was placed 2155 mm from the sample and an exposure time of 4 s was used.

The sample to detector distance and beam center coordinates on the detector were determined by a  $\text{LaB}_6$  NIST standard sample and using the software Fit2D [22]. The  $\text{LaB}_6$  standard was also used to estimate the instrumental peak broadening. A  $10^\circ$  wide sector of the two-dimensional raw-data was transformed into one-dimensional intensity vs “d-spacing” lineouts using Bragg’s law:  $2d \sin \theta = n\lambda$ , where the scattering angle,  $2\theta$ , is obtained from the sample to detector distance and the radial distance on the detector. The same sector of the two-dimensional raw-data is used for all samples. No deviation in diffraction rings with varied azimuthal angle was observed from the randomly oriented powder sample. By fitting pseudo-Voigt functions to the 1D data, the integrated intensity and full width at half maximum (FWHM) were extracted for further analysis with respect to isothermal annealing time.

For *ex situ* investigations, samples consisting of coated WC-Co substrates were annealed using the same experimental setup and the same heating and cooling rates as for the *in situ* experiments. The time and temperature for isothermal annealing were selected based on the results from the *in situ* experiments as explained in Section 3.1. The microstructure of as-deposited and annealed samples were studied by analytical transmission electron

microscopy (TEM), fast Fourier transform (FFT) and scanning TEM (STEM) using a FEI Tecnai G<sup>2</sup> TF 20 UT microscope operated at 200 kV and equipped with an EDS detector. Z-contrast STEM micrographs were obtained by a high-angle annular dark field (HAADF) detector operated with a camera length of 170 mm. The FFT images were obtained using the Gatan DigitalMicrograph™ software and the cross-sectional TEM samples were prepared by mechanical grinding followed by Ar-ion beam milling.

### 3. Results

#### 3.1 Phase evolution of *c*-TiCrAlN during annealing

**Figure 2** shows two-dimensional diffraction patterns from the  $\text{Ti}_{0.16}\text{Cr}_{0.36}\text{Al}_{0.48}\text{N}$  coating in its as-deposited state and at two different stages of isothermal annealing. In the exposure of the as-deposited TiCrAlN powder, only diffraction rings from *c*-TiCrAlN are observed. After ramping the temperature to 1150 °C, additional diffraction rings from the *h*-AlN phase appear, indicating decomposition of the *c*-TiCrAlN phase. Also, the positions of the diffraction rings from *c*-TiCrAlN shift to smaller angles due to thermal expansion. After isothermal annealing at 1150 °C for 278 min, diffraction rings from *h*-AlN, *c*-TiN and *c*-Cr phases are apparent. The presence of these phases suggests that a complete decomposition of the *c*-TiCrAlN phase into the equilibrium phases has occurred at this stage. As for  $\text{Ti}_{0.03}\text{Cr}_{0.38}\text{Al}_{0.59}\text{N}$ , a similar phase evolution was observed and detailed comparison between two alloys is shown in **Figure 3**.

Intensity versus *d*-spacing lineouts generated from the two-dimensional exposures are shown in **Figure 3** for selected annealing temperatures and times. For a better presentation of the decomposed phases, only a part of the data is shown, i.e. centered at the *c*-TiCrAlN 220 and *h*-AlN 100 peaks. The dashed lines mark the position of the binary bulk phases including

an approximate correction for thermal expansion at 1150 °C [20, 23-25]. Both  $\text{Ti}_{0.16}\text{Cr}_{0.36}\text{Al}_{0.48}\text{N}$  and  $\text{Ti}_{0.03}\text{Cr}_{0.38}\text{Al}_{0.59}\text{N}$  display only the c-TiCrAlN phase in the as-deposited state and the lattice constants,  $a(\text{Ti}_{0.16}\text{Cr}_{0.36}\text{Al}_{0.48}\text{N})=4.12 \text{ \AA}$  and  $a(\text{Ti}_{0.03}\text{Cr}_{0.38}\text{Al}_{0.59}\text{N})=4.10 \text{ \AA}$ , agree well with the estimated lattice parameters for such solid solutions [26]. During ramping to 1150 °C, the c-TiCrAlN peaks shift to higher d values because of thermal expansion.

In **Figure 3** (a), it is observed that during the first 30 min of isothermal annealing there are two shoulders on the c-TiCrAlN 220 peak contributing to the large peak broadening for the  $\text{Ti}_{0.16}\text{Cr}_{0.36}\text{Al}_{0.48}\text{N}$  sample. They are interpreted as domains enriched in c-AlN (c-(Ti)CrAlN) and c-TiN (c-TiCr(Al)N) respectively. In the lineouts from the  $\text{Ti}_{0.03}\text{Cr}_{0.38}\text{Al}_{0.59}\text{N}$  sample (**Figure 3**(c)), no shoulders corresponding to c-TiN or c-AlN enriched domains are observed. The two shoulders seen for  $\text{Ti}_{0.16}\text{Cr}_{0.36}\text{Al}_{0.48}\text{N}$  vanish after 30 min of isothermal annealing and the composition of the remaining cubic phase is close to c-Cr. An intermediate phase h-Cr<sub>2</sub>N was also observed (most clear at  $d\sim 2.12 \text{ \AA}$ ) during the early stage of decomposition ( $\sim 1000 \text{ °C}$  to 1150 °C), and N release during annealing was corroborated by a mass decrease observed by thermogravimetric analysis (not shown here). The h-Cr<sub>2</sub>N phase has been found during c-Cr phase formation in decomposed TiCrAlN and CrAlN coatings [16, 27].

The onset of decomposition is more clearly visualized by the FWHM of the c-TiCrAlN 220 peak as a function of isothermal annealing time shown in **Figure 4**, where peak width starts to increase at  $\sim 7$  min before reaching  $T_{\text{max}}$ , corresponding to  $\sim 1000 \text{ °C}$  for both coatings. For the as-deposited coatings ( $\sim 50$  min before isothermal annealing), the FWHM value ( $\sim 1.05 \text{ mrad}$ ) is similar for both samples and it decreases to  $\sim 0.75 \text{ mrad}$  during annealing at temperatures below 1000 °C. This is an effect of point defect (interstitials and vacancies) annihilation commonly observed during annealing of arc evaporated transition metal nitrides [28, 29]. Above 1000 °C and during the initial part of isothermal annealing the

FWHM increases to a maximum value of 1.17 mrad for  $\text{Ti}_{0.16}\text{Cr}_{0.36}\text{Al}_{0.48}\text{N}$  and 0.76 mrad for  $\text{Ti}_{0.03}\text{Cr}_{0.38}\text{Al}_{0.59}\text{N}$ . Considering that the same instrumental broadening prevails for both samples, a smaller coherent domain size, larger compositional variations, or higher microstrain is present in the  $\text{Ti}_{0.16}\text{Cr}_{0.36}\text{Al}_{0.48}\text{N}$  alloy compared to  $\text{Ti}_{0.03}\text{Cr}_{0.38}\text{Al}_{0.59}\text{N}$  during decomposition.

The FWHM (**Figure 4**) decreases to 0.42 mrad at ~20 min of isothermal annealing for  $\text{Ti}_{0.03}\text{Cr}_{0.38}\text{Al}_{0.59}\text{N}$  and ~60 min for  $\text{Ti}_{0.16}\text{Cr}_{0.36}\text{Al}_{0.48}\text{N}$ . Simultaneously, pure c-Cr, c-TiN and h-AlN have formed and grown. Diffraction signal from c-TiN appears in both samples during annealing though the intensity is small in the case of  $\text{Ti}_{0.03}\text{Cr}_{0.38}\text{Al}_{0.59}\text{N}$  since it only contains 3 at.% TiN. The first appearance of the h-AlN phase is best seen from the 100 diffraction signal ( $d \sim 2.7 \text{ \AA}$ ) which is first observed at 1000 °C in  $\text{Ti}_{0.03}\text{Cr}_{0.38}\text{Al}_{0.59}\text{N}$  and at 1150 °C for  $\text{Ti}_{0.16}\text{Cr}_{0.36}\text{Al}_{0.48}\text{N}$  (**Figure 3** (b, d)). In summary, both coatings contain the same phases (c-TiN, h-AlN and c-Cr) at the final stage of decomposition.

Samples annealed at  $T_{\text{max}}=1150 \text{ °C}$ , using heating and cooling rates of  $20 \text{ K min}^{-1}$  and hold times at  $T_{\text{max}}$  of 10 min ( $\text{Ti}_{0.16}\text{Cr}_{0.36}\text{Al}_{0.48}\text{N}$ ) and 0 min ( $\text{Ti}_{0.03}\text{Cr}_{0.38}\text{Al}_{0.59}\text{N}$ ) were chosen for TEM studies. The annealing time was selected such that 50 % of the total Al-content exists in the h-AlN phase (see section 3.2 below). **Figure 5** (a) and (b) shows the Z-contrast STEM micrographs of the annealed  $\text{Ti}_{0.16}\text{Cr}_{0.36}\text{Al}_{0.48}\text{N}$  and  $\text{Ti}_{0.03}\text{Cr}_{0.38}\text{Al}_{0.59}\text{N}$  sample, respectively. For both alloys, well-defined Al-rich grains (dark contrast) are accumulating along the boundary regions between Al-depleted grains of brighter contrast. A corresponding fast Fourier transform (FFT) of such a grain (not shown here) confirms its hexagonal structure, which is consistent with the h-AlN phase observed in the WAXS lineouts.

The inset of **Figure 5** (a) shows a STEM micrograph at higher magnification of the bright contrast grains in  $\text{Ti}_{0.16}\text{Cr}_{0.36}\text{Al}_{0.48}\text{N}$  marked with a dashed square. In this type of grain characteristic features of spinodal decomposition are observed, i.e. isostructural domains

formed by chemical fluctuations over a length scale of few nanometers [19]. The crystal structure was determined by HR-TEM and FFT to be cubic and the formed domains are consistent with the phases indicated as c-TiCr(Al)N and c-(Ti)CrAlN in WAXS lineouts. However, in  $\text{Ti}_{0.03}\text{Cr}_{0.38}\text{Al}_{0.59}\text{N}$  (**Figure 5** (b)) the bright grains show no internal contrast suggesting no chemical segregation within these grains, which is also confirmed by flat-line EDS line profiles (not shown). Instead these cubic grains display a homogeneous Cr-Al distribution.

### 3.2 Formation rate of h-AlN

From the lineouts in **Figure 3**, the h-AlN phase appears at lower temperature in  $\text{Ti}_{0.03}\text{Cr}_{0.38}\text{Al}_{0.59}\text{N}$  than  $\text{Ti}_{0.16}\text{Cr}_{0.36}\text{Al}_{0.48}\text{N}$ , indicating that formation of the h-AlN phase started at different annealing temperature. The kinetic analysis of the h-AlN formation is based on the Kolmogorov–Johnson–Mehl–Avrami (KJMA) equation, widely used to study the kinetics of phase transformations [30-32] and usually expressed as

$$f = 1 - e^{-kt^n} \quad (1)$$

Here,  $f$  is the transformed fraction of the phase of interest,  $k$  is a rate constant,  $t$  is time, and  $n$  is the Avrami constant, which is related to the nucleation mechanism. For example, under constant nucleation rate,  $n=4$  for three-dimensional growth while  $n$  decreases to 2 for one-dimensional growth [33, 34]. The rate constant ( $k$ ) depends on both nucleation and growth rates; it is therefore temperature dependent and has the form of an Arrhenius expression [33],

$$k = k_0 \exp\left(\frac{-E_a}{RT}\right), \quad (2)$$

where  $k_0$  is a pre-exponential constant,  $E_a$  is the activation energy,  $R$  is the molar gas constant and  $T$  is the absolute isothermal annealing temperature.

In the present study, the fraction of h-AlN formed is determined from the intensity of the diffraction signal. From the transformed fraction as a function of annealing time, the activation energy required to form this phase can be extracted using Eqs. (1) and (2). To determine  $E_a$  for the formation of h-AlN, the integrated intensity of the h-AlN 100 diffraction peak was determined as a function of annealing time at  $T_{\max}$ . The integrated intensities were normalized and transformed to h-AlN fraction as a function of time following the procedure reported elsewhere [20]. First, the integrated intensity of the h-AlN 100 peak recorded during annealing is normalized with the integrated intensity of the c-TiCrAlN 200 peak recorded prior to initiating the heat treatment to account for varying powder amounts between measurements. Next, the transformed fraction of h-AlN is determined by assuming that after annealing for sufficiently long time at the highest  $T_{\max}$  such that no new h-AlN is formed the transformation is complete, i.e. all Al-atoms are at this point in the h-AlN phase and any AlN dissolved in c-TiCrN is ignored. **Figure 6** shows the fraction of transformed h-AlN as a function of isothermal annealing time for  $\text{Ti}_{0.16}\text{Cr}_{0.36}\text{Al}_{0.48}\text{N}$  and  $\text{Ti}_{0.03}\text{Cr}_{0.38}\text{Al}_{0.59}\text{N}$  for three  $T_{\max}$ . For both  $T_{\max}=1050$  °C (red) and  $1150$  °C (dark blue) the rate of forming h-AlN is faster in the case of  $\text{Ti}_{0.03}\text{Cr}_{0.38}\text{Al}_{0.59}\text{N}$  compared to  $\text{Ti}_{0.16}\text{Cr}_{0.36}\text{Al}_{0.48}\text{N}$ . For  $T_{\max}=1150$  °C, the formation of the h-AlN phase is completed after ~50 min of isothermal annealing time for  $\text{Ti}_{0.03}\text{Cr}_{0.38}\text{Al}_{0.59}\text{N}$  while it takes almost 200 min to reach the fully transformed state for  $\text{Ti}_{0.16}\text{Cr}_{0.36}\text{Al}_{0.48}\text{N}$ .

To extract the activation energy, Eq. (1) is first rewritten by applying the logarithm twice to yield

$$\ln(-\ln(1 - f)) = \ln k + n \cdot \ln t \quad (3)$$

Based on Eq. (3), a plot of  $\ln(-\ln(1 - f))$  versus  $\ln(t)$  should result in a straight line, which intercepts the y-axis at  $\ln k$  and has a slope corresponding to  $n$ . The plot for  $\text{Ti}_{0.16}\text{Cr}_{0.36}\text{Al}_{0.48}\text{N}$  is shown in **Figure 7** (a). Using Eq. (3),  $\ln k$  and  $n$  values for three different

isothermal annealing temperatures were obtained for each sample, respectively. By taking the logarithm of Eq. (2) we get an expression relating the obtained  $\ln k$  to the activation energy,

$$\ln k = \ln k_0 - \frac{E_a}{RT} \quad (4)$$

Thus, the slope of a fitted line to the plot of  $\ln k$  versus  $(1/T)$  gives the activation energy and the y-axis intercept is the logarithm of the pre-exponential constant. **Figure 7** (b) shows these plots and the corresponding linear fits of Eq. (4) for both  $\text{Ti}_{0.16}\text{Cr}_{0.36}\text{Al}_{0.48}\text{N}$  and  $\text{Ti}_{0.03}\text{Cr}_{0.38}\text{Al}_{0.59}\text{N}$ . A clear difference in slope corresponds to the large difference in activation energy for the transformation to h-AlN between the two coatings. The poorer fit in  $\text{Ti}_{0.03}\text{Cr}_{0.38}\text{Al}_{0.59}\text{N}$  at the highest  $T_{\max}=1150$  °C due to fast transformation rate of h-AlN results in a larger error of the extracted parameters for this sample. However, the difference in  $E_a$  for the two samples is statistically significant. The resulting values of the activation energy are for  $\text{Ti}_{0.16}\text{Cr}_{0.36}\text{Al}_{0.48}\text{N}$   $304 \pm 7$  kJ/mol ( $3.17 \pm 0.07$  eV/atom) and for  $\text{Ti}_{0.03}\text{Cr}_{0.38}\text{Al}_{0.59}\text{N}$   $88 \pm 36$  kJ/mol ( $0.92 \pm 0.38$  eV/atom). The extracted parameters; the activation energy and Avrami constant ( $n$ ), are presented in **Table 1** along with the results for  $\text{Ti}_{1-x}\text{Al}_x\text{N}$  [20] obtained by the same procedure. The Avrami constant does not vary much between different alloys and thus its contribution to the differences in transformation rate is small. This is underlined in the literature where similar Avrami constants have been reported for a range of phase transformations under varying conditions [35-37]. The modified KJMA equation, including an impingement parameter whose value depends on the nucleation site (e.g. grain boundary or bulk site) [20, 38] has also been tested and it results in only small changes in the activation energies when the impingement parameter ( $\epsilon$ ) is varied in the range of 0.1-3. Hence, those results are not presented here.

### Table 1

**Activation energy and the Avrami constant from Eq. (2) for the h-AlN transformation.**

**The values of  $E_a$  for  $Ti_{0.36}Al_{0.64}N$  and  $Ti_{0.55}Al_{0.45}N$  are taken from Ref. [20].**

	Activation energy, $E_a$ (kJ/mol)	Avrami constant, $n$
$Ti_{0.16}Cr_{0.36}Al_{0.48}N$	$304 \pm 7$	0.67
$Ti_{0.03}Cr_{0.38}Al_{0.59}N$	$88 \pm 36$	0.43
$Ti_{0.36}Al_{0.64}N$	$320 \pm 10$	0.75
$Ti_{0.55}Al_{0.45}N$	$350 \pm 40$	0.77

The transformation rate depends on nucleation rate as well as growth rate. As the peak broadening (FWHM) is related to grain size, the change of FWHM with annealing time gives an estimation of the growth rate. **Figure 8** shows how the FWHM value of the h-AlN 100 peak changes as a function of isothermal annealing time at  $T_{max}=1050$  °C and 1150 °C for  $Ti_{0.16}Cr_{0.36}Al_{0.48}N$  and  $Ti_{0.03}Cr_{0.38}Al_{0.59}N$ . The approximate grain size was calculated from the peak broadening by the Scherrer equation [39], where the peak broadening was first corrected for instrumental broadening (0.25 mrad). From the isothermal annealing at  $T_{max}=1050$  °C, we can clearly observe that although the h-AlN grains in  $Ti_{0.16}Cr_{0.36}Al_{0.48}N$  are smaller than in  $Ti_{0.03}Cr_{0.38}Al_{0.59}N$  at the start ( $t=0$ ) of the isothermal annealing, the h-AlN grains end up with approximately the same grain size (33 nm for  $Ti_{0.03}Cr_{0.38}Al_{0.59}N$ , 31 nm for  $Ti_{0.16}Cr_{0.36}Al_{0.48}N$ ) at the end (~180 min) of the isothermal annealing process. When increasing  $T_{max}$  to 1150 °C, with almost the same size of h-AlN grains in both TiCrAlN alloys at the start ( $t=0$ ) of isothermal annealing, the h-AlN mean grain size in  $Ti_{0.16}Cr_{0.36}Al_{0.48}N$  is clearly larger after ~15 min of isothermal annealing. This difference can have two origins: (i) a higher h-AlN grain growth rate in  $Ti_{0.16}Cr_{0.36}Al_{0.48}N$  than  $Ti_{0.03}Cr_{0.38}Al_{0.59}N$ , especially at higher annealing

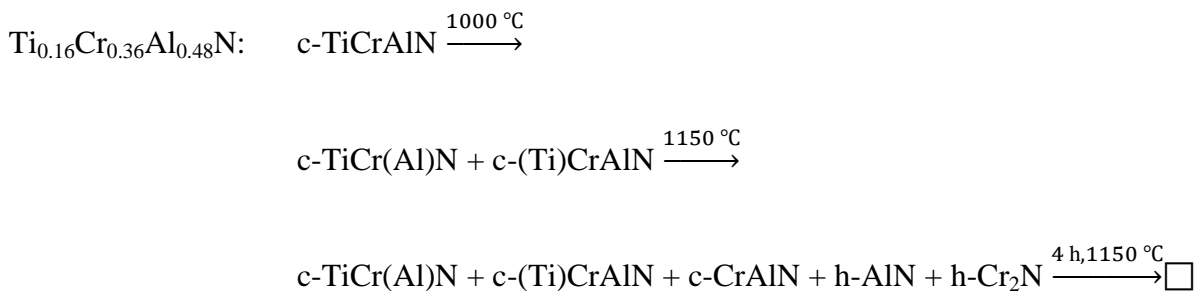
temperatures; or (ii) a higher h-AlN nucleation rate in  $\text{Ti}_{0.03}\text{Cr}_{0.38}\text{Al}_{0.59}\text{N}$ , resulting in lower average grain size of h-AlN compared with  $\text{Ti}_{0.16}\text{Cr}_{0.36}\text{Al}_{0.48}\text{N}$ .

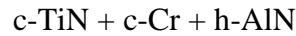
## 4. Discussion

### 4.1 Phase and microstructure evolution during annealing

In the as-deposited state, no other phases except the c-TiCrAlN phase are found in the coatings. Both coatings exhibit columnar growth with similar grain size based on cross-sectional images of the coatings. The FWHM of the c-TiCrAlN peak is similar for both as-deposited coatings indicating that the grain size and defect density is similar in both coatings. During annealing at  $T < 1000$  °C, annihilation of point defects occur to a similar extent for both compositions. The observed phase evolution during annealing agrees well with previous studies of TiCrAlN by *ex situ* x-ray diffraction [16, 17], with the end products being c-TiN, c-Cr and h-AlN. Also the intermediate phase (h-Cr<sub>2</sub>N), forming before transformation to c-Cr, exhibits similar behavior in terms of formation and decomposition temperatures despite using different heating cycles in this study compared to what has been reported previously [17, 40]. For both  $\text{Ti}_{0.16}\text{Cr}_{0.36}\text{Al}_{0.48}\text{N}$  and  $\text{Ti}_{0.03}\text{Cr}_{0.38}\text{Al}_{0.59}\text{N}$ , the formed phases exist in both coatings but with varying amount and growth rate, which is an effect of the different alloy compositions.

The decomposition routes of the two TiCrAlN alloys can be written as





Studies of  $c\text{-Ti}_x\text{Cr}_{1-x}\text{Al}_{0.61}\text{N}$  alloys[17], have shown two co-occurring mechanisms of decomposition: spinodal decomposition of the  $c\text{-TiCrAlN}$  phase and direct precipitation of  $h\text{-AlN}$  from the  $c\text{-(Ti)CrAlN}$  phase. It was found that increasing the Ti-content while keeping the Al-content constant promotes spinodal decomposition. In this work, both Ti- and Al-content are changed between the coatings which also influence the decomposition behavior, although theoretical studies predict that the driving force for spinodal decomposition is similar for  $\text{Ti}_{0.03}\text{Cr}_{0.38}\text{Al}_{0.59}\text{N}$  and  $\text{Ti}_{0.16}\text{Cr}_{0.36}\text{Al}_{0.48}\text{N}$ [26].

In the case of the  $\text{Ti}_{0.16}\text{Cr}_{0.36}\text{Al}_{0.48}\text{N}$  alloy our experimental findings show an evolution of a compositional modulated microstructure consistent with spinodal decomposition. In contrast, the low Ti-content  $\text{Ti}_{0.03}\text{Cr}_{0.38}\text{Al}_{0.59}\text{N}$  alloy does not display the same behavior. Instead, at  $1000\text{ }^\circ\text{C}$ , nucleation and growth of three major phases occur:  $h\text{-AlN}$  and two cubic phases,  $c\text{-TiN}$  and  $c\text{-CrAlN}$ . At this stage, some of the Ti-depleted  $c\text{-TiCrAlN}$  phase remains. The decomposition results in a refinement of the microstructure, which causes a slight x-ray peak broadening compared with  $\text{Ti}_{0.16}\text{Cr}_{0.36}\text{Al}_{0.48}\text{N}$ . Complete separation into  $h\text{-AlN}$ ,  $c\text{-TiN}$  and  $c\text{-CrAlN}$  occurs at a later stage of annealing ( $1150\text{ }^\circ\text{C}$ ). For both alloys,  $h\text{-AlN}$  is expected to precipitate from the  $c\text{-CrAlN}$  phase [27, 40]. The earlier observation of  $h\text{-AlN}$  in the low Ti-content sample indicates that  $c\text{-CrAlN}$  forms earlier in this sample.

With approximately similar amount of h-AlN (i.e. when the h-AlN phase contains 50 % of the total amount of Al in the sample), the h-AlN grains tend to accumulate in grain boundary areas for both samples (see **Figure 5**). Comparing with previous results for c-Ti<sub>0.11</sub>Cr<sub>0.28</sub>Al<sub>0.61</sub>N [17], with a similar alloy composition as in the current study, precipitation of h-AlN along grain boundaries was found to occur for high annealing temperatures (1000 °C), thus in agreement with the precipitation behavior of h-AlN grains found here. Though at an earlier stage of decomposition (annealing at 900 °C) the segregation of Al to grain boundaries was less obvious [17]. This suggests that h-AlN precipitates mainly at grain boundaries despite the preceding spinodal decomposition in the alloy, which is actually similar to TiAlN [2].

The size of h-AlN grains in the Ti<sub>0.03</sub>Cr<sub>0.38</sub>Al<sub>0.59</sub>N sample annealed at 1050 °C estimated from the STEM micrograph is 30-50 nm, which is slightly larger than the 28 nm grain size determined by x-ray peak broadening analysis. For the Ti<sub>0.16</sub>Cr<sub>0.36</sub>Al<sub>0.48</sub>N sample at the same temperature, the h-AlN grain size is estimated to 50-75 nm from STEM and 35 nm from x-ray peak broadening analysis. These differences suggest subgrain formation in the h-AlN, perhaps due to entrapped Cr and Ti atoms or coalescence of slightly misaligned h-AlN grains. The subgrain formation is more pronounced in the Ti<sub>0.16</sub>Cr<sub>0.36</sub>Al<sub>0.48</sub>N sample.

#### *4.2 Kinetics of h-AlN formation*

The large difference in formation rate of h-AlN between the two alloys suggests that the formation rate depends on the decomposition route, where the occurrence of spinodal decomposition in one of the alloys affects the transformation rate. And since the h-AlN phase forms from CrAlN for both alloys, formation of CrAlN then limits the h-AlN transformation rate.

In the Ti<sub>0.03</sub>Cr<sub>0.38</sub>Al<sub>0.59</sub>N coating, the c-CrAlN grain size is already in the order of 50-100 nm after ramping to 1150 °C without hold period. In contrast, the c-(Ti)CrAlN domains

formed during spinodal decomposition of  $\text{Ti}_{0.16}\text{Cr}_{0.36}\text{Al}_{0.48}\text{N}$  remain small for longer annealing times. After 10 min at 1150 °C their size is still just a few nm. Further, Forsén et al. [8] have shown that better lattice matching can be achieved between the two cubic phases in the presence of Cr causing a reduced coherency strain and thereby increasing the stability. The domains can then grow larger while still remaining coherent [41]. This delays the transformation to h-AlN, resulting in lower transformation rates compared to TiAlN [20]. Comparing the two TiCrAlN alloys, the Cr containing domains we observe here with coherent interfaces in  $\text{Ti}_{0.16}\text{Cr}_{0.36}\text{Al}_{0.48}\text{N}$  have a lower driving force for Al migration to the grain boundaries where h-AlN is formed. The net result is that the CrAlN domains within the fine microstructure caused by spinodal decomposition are more stable than the larger CrAlN grains in  $\text{Ti}_{0.03}\text{Cr}_{0.38}\text{Al}_{0.59}\text{N}$ .

The formation of h-AlN occurs by nucleation and growth, while both nucleation and growth rates affect the overall transformation rate. Despite a slower transformation rate to h-AlN of the  $\text{Ti}_{0.16}\text{Cr}_{0.36}\text{Al}_{0.48}\text{N}$ , it displays larger h-AlN grains. It leads us to conclude that the h-AlN nucleation rate is higher for  $\text{Ti}_{0.03}\text{Cr}_{0.38}\text{Al}_{0.59}\text{N}$  than  $\text{Ti}_{0.16}\text{Cr}_{0.36}\text{Al}_{0.48}\text{N}$ . The lower nucleation rate for  $\text{Ti}_{0.16}\text{Cr}_{0.36}\text{Al}_{0.48}\text{N}$  is likely caused by the relatively more stable c-CrAlN domains surrounded by c-TiCrN, compared to c-CrAlN with small amounts of dissolved Ti in  $\text{Ti}_{0.03}\text{Cr}_{0.38}\text{Al}_{0.59}\text{N}$ . Hence, the migration of Al is shifted to higher temperatures, which gives higher mobility and enlarges the critical radius of an h-AlN nucleus, promoting growth over nucleation.

The two different samples have different activation energy for the formation of h-AlN. The value for the  $\text{Ti}_{0.16}\text{Cr}_{0.36}\text{Al}_{0.48}\text{N}$  (304 kJ/mol) is comparable to what has been reported for TiAlN-alloys without Cr. In contrast, the activation energy recorded for  $\text{Ti}_{0.03}\text{Cr}_{0.38}\text{Al}_{0.59}\text{N}$  is more than a factor of three lower, i.e. 88 kJ/mol. While there is a lower certainty for the activation energy value for  $\text{Ti}_{0.03}\text{Cr}_{0.38}\text{Al}_{0.59}\text{N}$ , it is significantly lower than the value for

$\text{Ti}_{0.16}\text{Cr}_{0.36}\text{Al}_{0.48}\text{N}$  and for  $\text{TiAlN}$ . It adds to the argument that the  $\text{CrAlN}$  phase is stabilized by the coherency strain imposed by the surrounding  $c\text{-TiCrN}$  phase.

The similar value of the activation energy for  $\text{Ti}_{0.16}\text{Cr}_{0.36}\text{Al}_{0.48}\text{N}$  and the two  $\text{TiAlN}$  alloys (see **Table 1**) is surprising as the phase transformation is different in the case of  $\text{TiCrAlN}$  and  $\text{TiAlN}$ . In  $\text{TiAlN}$ , pure  $c\text{-AlN}$  domains transform to  $h\text{-AlN}$  while in  $\text{TiCrAlN}$   $h\text{-AlN}$  precipitates from the  $c\text{-CrAlN}$  domains. On the other hand, the activation energy for  $\text{Ti}_{0.16}\text{Cr}_{0.36}\text{Al}_{0.48}\text{N}$  and for  $\text{TiAlN}$  is in the same order as the activation energy for diffusion in  $\text{TiAlN}$  alloys [3, 19], which implies that the  $h\text{-AlN}$  formation rate may be diffusion controlled in both cases. Formation of  $h\text{-AlN}$  from  $c\text{-CrAlN}$  [8, 17, 41] or  $c\text{-AlN}$  [5, 42, 43] involves migrating Al atoms that must overcome similar energy barriers in the decomposed cubic matrix, which likely explains the small difference in activation energy. While the structure of Al-rich domains is similar for  $\text{TiAlN}$  and  $\text{Ti}_{0.16}\text{Cr}_{0.36}\text{Al}_{0.48}\text{N}$ , the  $c\text{-CrAlN}$  grains in  $\text{Ti}_{0.03}\text{Cr}_{0.38}\text{Al}_{0.59}\text{N}$  are not confined in a nanoscale compositionally modulated structure. The different microstructure yields another diffusion path, which is responsible for the deviating activation energy found for this sample.

The activation energy for lattice diffusion and grain boundary diffusion can differ by up to three times as was found for Al thin films [44] and metal diffusions in nitride films [45, 46], where the activation energy for grain boundary diffusion (30-115 kJ/mol) is in the range of what is found here for formation of  $h\text{-AlN}$  in  $\text{Ti}_{0.03}\text{Cr}_{0.38}\text{Al}_{0.59}\text{N}$ . As evident from the STEM micrographs in **Figure 5**,  $h\text{-AlN}$  precipitates at grain boundaries for both  $\text{TiCrAlN}$  alloys. The supply of Al to the grain boundaries is likely dependent on the location of  $\text{AlN}$ -rich domains, which for  $\text{Ti}_{0.03}\text{Cr}_{0.38}\text{Al}_{0.59}\text{N}$ , the  $c\text{-CrAlN}$  grains are in direct connection to the grain boundaries, while in  $\text{Ti}_{0.16}\text{Cr}_{0.36}\text{Al}_{0.48}\text{N}$  they are located within the nanoscale microstructure originating from spinodal decomposition. Thus, precipitations of  $h\text{-AlN}$  at grain boundaries

take place in  $\text{Ti}_{0.03}\text{Cr}_{0.38}\text{Al}_{0.59}\text{N}$  while lattice diffusion limits the formation rate of h-AlN in  $\text{Ti}_{0.16}\text{Cr}_{0.36}\text{Al}_{0.48}\text{N}$ , which determines the large difference in the activation energy.

In summary, the rate of h-AlN formation in TiCrAlN alloys is related to the stability of the c-CrAlN phase, which primarily is governed by the surrounding microstructure. It results in different transformation kinetics where coherency strain confines the c-CrAlN domains generated during spinodal decomposition and decreases the transformation rate in comparison to precipitation from larger incoherent c-CrAlN grains. Further, precipitations of h-AlN from c-CrAlN grains at grain boundaries results in high transformation rates due to the low activation energy for diffusion of Al atoms.

## 5. Conclusion

The decomposition mechanism and the kinetics of the decomposition process in  $\text{Ti}_x\text{Cr}_{1-x}\text{Al}_{1-x}\text{N}$  alloys with varying Ti content were investigated by *in situ* x-ray scattering during annealing. The same phases form during annealing in both samples, while the decomposition route depends on the Ti-content. For high Ti-content  $\text{Ti}_{0.16}\text{Cr}_{0.36}\text{Al}_{0.48}\text{N}$ , spinodal decomposition occurs that results in nanoscale, coherent domains of c-(Ti)CrAlN and c-TiCr(Al)N. In low Ti-content  $\text{Ti}_{0.03}\text{Cr}_{0.38}\text{Al}_{0.59}\text{N}$ , c-CrAlN, c-TiN and h-AlN forms through nucleation and growth.

The formation rate of h-AlN is determined by the formation and the stability of c-CrAlN domains. With low Ti-content, nucleation and growth results in large, pure c-CrAlN grains forming in an early stage of decomposition. Also, h-AlN precipitates from such c-CrAlN grains with a high rate due to high diffusivity along grain boundaries. In contrast, the CrAlN domains forming during spinodal decomposition in the high Ti-content coating are stabilized by lattice coherency with the surrounding c-TiCrN domains. The formation of h-

AlN is limited by bulk diffusion of Al to grain boundaries where h-AlN forms. Combining these variations during decomposition, higher activation energy for h-AlN formation is found for the high Ti-content TiCrAlN alloy.

## **Acknowledgment**

We acknowledge the financial support from EU's Erasmus-Mundus graduate school in Material Science and Engineering (DocMASE), the Swedish Research Council VR (621-2012-4401) and Röntgen-Ångström Cluster grant that includes access to Petra III, Swedish Foundation for Strategic Research, SSF (RMA08-0069), Swedish government strategic research area grant AFM – SFO MatLiU (2009-00971), and VINNOVA (M – Era.net project 2013-02355). We also thank Dr. Jeremy Schroeder for assistance with synchrotron equipment set-ups and data collection and Dr. Jianqiang Zhu for (S)TEM investigations.

## **References**

- [1] A. Hörling, L. Hultman, M. Odén, J. Sjöln, L. Karlsson, Mechanical properties and machining performance of Ti<sub>1-x</sub>Al<sub>x</sub>N-coated cutting tools, *Surface & coatings technology*, 191 (2005) 384-392.
- [2] R. Rachbauer, S. Massl, E. Stergar, D. Holec, D. Kiener, J. Keckes, J. Patscheider, M. Stiefel, H. Leitner, P.H. Mayrhofer, Decomposition pathways in age hardening of Ti-Al-N films, *Journal of Applied Physics*, 110 (2011) 023515.
- [3] P.H. Mayrhofer, A. Hörling, L. Karlsson, J. Sjöln, T. Larsson, C. Mitterer, L. Hultman, Self-organized nanostructures in the Ti–Al–N system, *Applied Physics Letters*, 83 (2003) 2049.

- [4] M. Odén, L. Rogström, A. Knutsson, M.R. Terner, P. Hedström, J. Almer, J. Ilavsky, In situ small-angle x-ray scattering study of nanostructure evolution during decomposition of arc evaporated TiAlN coatings, *Applied Physics Letters*, 94 (2009) 053114.
- [5] L. Rogström, J. Ullbrand, J. Almer, L. Hultman, B. Jansson, M. Odén, Strain evolution during spinodal decomposition of TiAlN thin films, *Thin Solid Films*, 520 (2012) 5542-5549.
- [6] M.A. Davies, T. Ueda, R. M'Saoubi, B. Mullany, A.L. Cooke, On The Measurement of Temperature in Material Removal Processes, *CIRP Annals - Manufacturing Technology*, 56 (2007) 581-604.
- [7] A. Knutsson, M.P. Johansson, L. Karlsson, M. Odén, Thermally enhanced mechanical properties of arc evaporated  $\text{Ti}_{0.34}\text{Al}_{0.66}\text{N}/\text{TiN}$  multilayer coatings, *Journal of Applied Physics*, 108 (2010) 044312.
- [8] R. Forsén, N. Ghafoor, M. Odén, Coherency strain engineered decomposition of unstable multilayer alloys for improved thermal stability, *Journal of Applied Physics*, 114 (2013) 244303
- [9] K. Kutschej, N. Fateh, P.H. Mayrhofer, M. Kathrein, P. Polcik, C. Mitterer, Comparative study of Ti1-xAlxN coatings alloyed with Hf, Nb, and B, *Surface & coatings technology*, 200 (2005) 113-117.
- [10] L. Chen, D. Holec, Y. Du, P.H. Mayrhofer, Influence of Zr on structure, mechanical and thermal properties of Ti-Al-N, *Thin Solid Films*, 519 (2011) 5503-5510.
- [11] D. Holec, L. Zhou, R. Rachbauer, P.H. Mayrhofer, Alloying-related trends from first principles: An application to the Ti-Al-X-N system, *Journal of Applied Physics*, 113 (2013) 113510.
- [12] H.W. Hugosson, H. Högberg, M. Algren, M. Rodmar, T.I. Selinder, Theory of the effects of substitutions on the phase stabilities of Ti1-xAlxN, *Journal of Applied Physics*, 93 (2003) 4505-4511.
- [13] S.G. Harris, E.D. Doyle, A.C. Vlasveld, J. Audy, J.M. Long, D. Quick, Influence of chromium content on the dry machining performance of cathodic arc evaporated TiAlN coatings, *Wear*, 254 (2003) 185-194.
- [14] Z.F. Zhou, P.L. Tam, P.W. Shum, K.Y. Li, High temperature oxidation of CrTiAlN hard coatings prepared by unbalanced magnetron sputtering, *Thin Solid Films*, 517 (2009) 5243-5247.
- [15] A.I. Kovalev, D.L. Wainstein, A.Y. Rashkovskiy, G.S. Fox-Rabinovich, K. Yamamoto, S. Veldhuis, M. Aguirre, B.D. Beake, Impact of Al and Cr alloying in TiN-based PVD coatings on cutting performance during machining of hard to cut materials, *Vacuum*, 84 (2009) 184-187.
- [16] R. Forsén, M. Johansson, M. Odén, N. Ghafoor, Decomposition and phase transformation in TiCrAlN thin coatings, *Journal of Vacuum Science & Technology A: Vacuum, Surfaces, and Films*, 30 (2012) 061506.
- [17] R. Forsén, M.P. Johansson, M. Odén, N. Ghafoor, Effects of Ti alloying of AlCrN coatings on thermal stability and oxidation resistance, *Thin Solid Films*, 534 (2013) 394-402.
- [18] B. Alling, T. Marten, I.A. Abrikosov, A. Karimi, Comparison of thermodynamic properties of cubic Cr1-xAlxN and Ti1-xAlxN from first-principles calculations, *Journal of Applied Physics*, 102 (2007).
- [19] A. Knutsson, J. Ullbrand, L. Rogström, N. Norrby, L.J.S. Johnson, L. Hultman, J. Almer, M.P. Johansson Jöesaar, B. Jansson, M. Odén, Microstructure evolution during the isostructural decomposition of TiAlN—A combined in-situ small angle x-ray scattering and phase field study, *Journal of Applied Physics*, 113 (2013) 213518.

- [20] N. Norrby, L. Rogström, M.P. Johansson-Jöesaar, N. Schell, M. Odén, In situ X-ray scattering study of the cubic to hexagonal transformation of AlN in Ti<sub>1-x</sub>Al<sub>x</sub>N, *Acta Materialia*, 73 (2014) 205-214.
- [21] R. Forsén, I.C. Schramm, P.O.A. Persson, F. Mucklich, M. Odén, N. Ghafoor, Nanostructuring and coherency strain in multicomponent hard coatings, *Apl Mater*, 2 (2014) 116104.
- [22] A P Hammersley, `FIT2D: An Introduction and Overview, ESRF Internal Report, ESRF97HA02T, (1997).
- [23] Joint Committee of Powder Diffraction Standards (JCPDS)—International Centre for Diffraction Data, 1998, Card No. 25-1133.
- [24] Joint Committee of Powder Diffraction Standards (JCPDS)—International Centre for Diffraction Data, 1998, Card No. 38-1420.
- [25] Joint Committee of Powder Diffraction Standards (JCPDS)—International Centre for Diffraction Data, 1998, Card No. 89-4055.
- [26] H. Lind, R. Forsén, B. Alling, N. Ghafoor, F. Tasnadi, M.P. Johansson, I.A. Abrikosov, M. Odén, Improving thermal stability of hard coating films via a concept of multicomponent alloying, *Applied Physics Letters*, 99 (2011) 5090.
- [27] P.H. Mayrhofer, H. Willmann, A.E. Reiter, Structure and phase evolution of Cr–Al–N coatings during annealing, *Surface and Coatings Technology*, 202 (2008) 4935-4938.
- [28] M. Odén, J. Almer, G. Håkansson, M. Olsson, Microstructure–property relationships in arc-evaporated Cr–N coatings, *Thin Solid Films*, 377–378 (2000) 407-412.
- [29] K. Grönhagen, J. Ågren, M. Odén, Phase-field modelling of spinodal decomposition in TiAlN including the effect of metal vacancies, *Scripta Materialia*, 95 (2015) 42-45.
- [30] M. Avrami, Kinetics of Phase Change. I General Theory, *The Journal of Chemical Physics*, 7 (1939) 1103.
- [31] M. Avrami, Kinetics of Phase Change. II Transformation-Time Relations for Random Distribution of Nuclei, *The Journal of Chemical Physics*, 8 (1940) 212.
- [32] M. Avrami, Granulation, Phase Change, and Microstructure Kinetics of Phase Change. III, *The Journal of Chemical Physics*, 9 (1941) 177.
- [33] D.A. Porter, K.E. Easterling, *Phase Transformations in Metals and Alloys*, Third Edition (Revised Reprint), Taylor & Francis, 1992.
- [34] T. Pradell, D. Crespo, N. Clavaguera, M.T. Clavaguera-Mora, Diffusion controlled grain growth in primary crystallization: Avrami exponents revisited, *J Phys-Condens Mat*, 10 (1998) 3833-3844.
- [35] E.J. Mittemeijer, I.A. Wierszylowski, The Isothermal and Nonisothermal Kinetics of Tempering Iron-Carbon and Iron-Nitrogen Martensites and Austenites, *Z Metallkd*, 82 (1991) 419-429.
- [36] E.J. Mittemeijer, Analysis of the Kinetics of Phase-Transformations, *J Mater Sci*, 27 (1992) 3977-3987.

- [37] A. Khatibi, J. Lu, J. Jensen, P. Eklund, L. Hultman, Phase transformations in face centered cubic (Al<sub>0.32</sub>Cr<sub>0.68</sub>)<sub>2</sub>O<sub>3</sub> thin films, *Surface and Coatings Technology*, 206 (2012) 3216-3222.
- [38] E.A. Jägler, E.J. Mittemeijer, The kinetics of grain-boundary nucleated phase transformations: Simulations and modelling, *Acta Materialia*, 59 (2011) 5775-5786.
- [39] U.t.G.t. Königliche Gesellschaft der Wissenschaften zu Göttingen, Nachrichten von der Königl. Gesellschaft der Wissenschaften und der G.A. Universität zu Göttingen, in, Dieterichschen Buchhandlung, Göttingen, 1845.
- [40] H. Willmann, P.H. Mayrhofer, P.O.Å. Persson, A.E. Reiter, L. Hultman, C. Mitterer, Thermal stability of Al–Cr–N hard coatings, *Scripta Materialia*, 54 (2006) 1847-1851.
- [41] H. Willmann, P.H. Mayrhofer, L. Hultman, C. Mitterer, Hardness evolution of Al-Cr-N coatings under thermal load, *Journal of Materials Research*, 23 (2008) 2880-2885.
- [42] I.A. Abrikosov, A. Knutsson, B. Alling, F. Tasnadi, H. Lind, L. Hultman, M. Odén, Phase Stability and Elasticity of TiAlN, *Materials*, 4 (2011) 1599-1618.
- [43] A. Hörling, L. Hultman, M. Odén, J. Sjöln, L. Karlsson, Thermal stability of arc evaporated high aluminum-content Ti<sub>1-x</sub>Al<sub>x</sub>N thin films, *Journal of Vacuum Science & Technology A*, 20 (2002) 1815-1823.
- [44] A. Jankowski, J. Ferreira, J. Hayes, Activation energies of grain growth mechanisms in aluminum coatings, *Thin Solid Films*, 491 (2005) 61-65.
- [45] C. Engstrom, J. Birch, L. Hultman, C. Lavoie, C. Cabral, J.L. Jordan-Sweet, J.R.A. Carlsson, Interdiffusion studies of single crystal TiN/NbN superlattice thin films, *J Vac Sci Technol A*, 17 (1999) 2920-2927.
- [46] G.I. Grigorov, K.G. Grigorov, M. Stoyanova, J.L. Vignes, J.P. Langeron, P. Denjean, Aluminum Diffusion in Titanium Nitride Films - Efficiency of Tin Barrier Layers, *Appl Phys a-Mater*, 57 (1993) 195-197.

## Figures

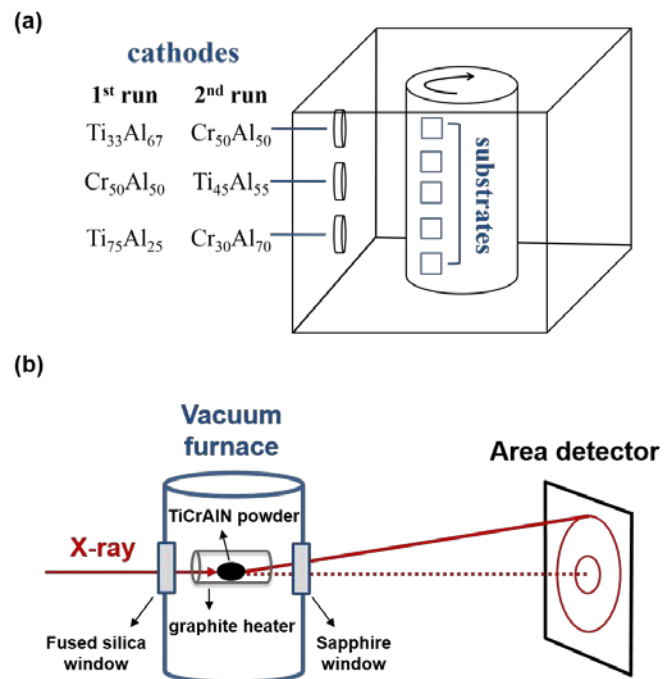


**Figure 1** (a) Deposition system for TiCrAlN coatings by cathodic arc evaporation (b) The *in situ* WAXS measurement set-up during high temperature annealing.

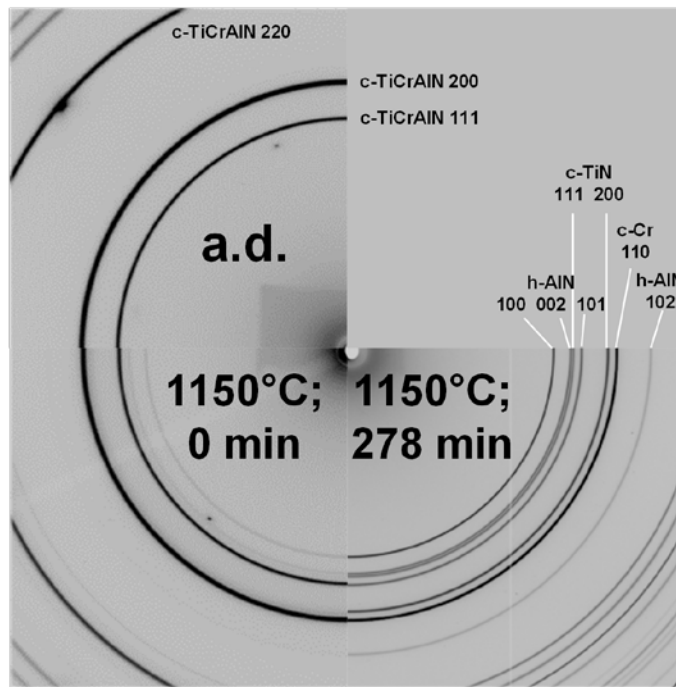


**Figure 2 Two-dimensional x-ray diffraction patterns from the  $\text{Ti}_{0.16}\text{Cr}_{0.36}\text{Al}_{0.48}\text{N}$  coating in its as-deposited (a.d.) state and during isothermal annealing at 1150 °C with holding time of 0 min and 278 min.**

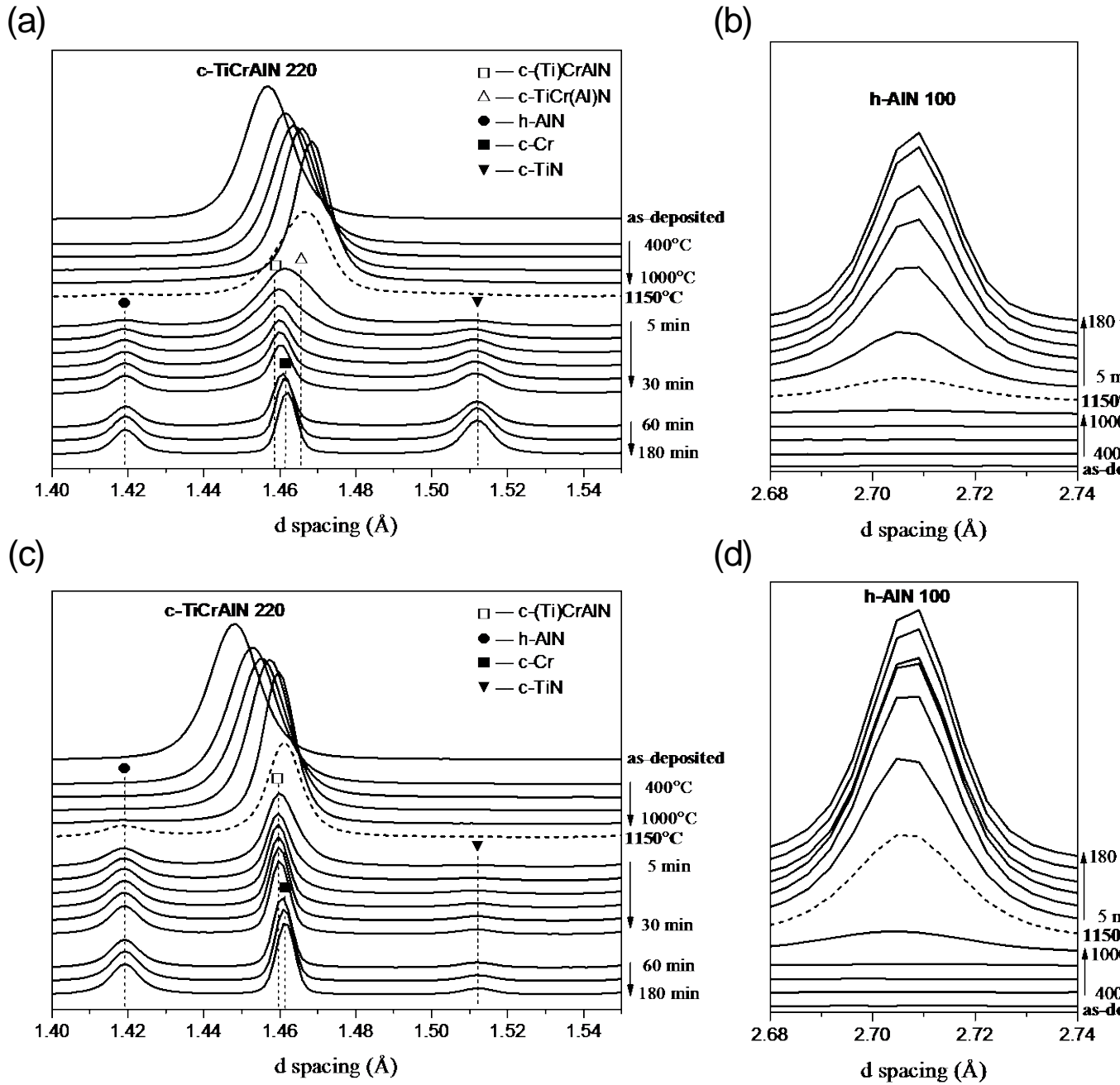


Figure 3 Lineouts from the as-deposited sample and at selected annealing temperatures while ramping to 1150 °C (dashed line) and subsequent holding for (a, b)  $\text{Ti}_{0.16}\text{Cr}_{0.36}\text{Al}_{0.48}\text{N}$  and (c, d)  $\text{Ti}_{0.03}\text{Cr}_{0.38}\text{Al}_{0.59}\text{N}$ , for different d spacing intervals.

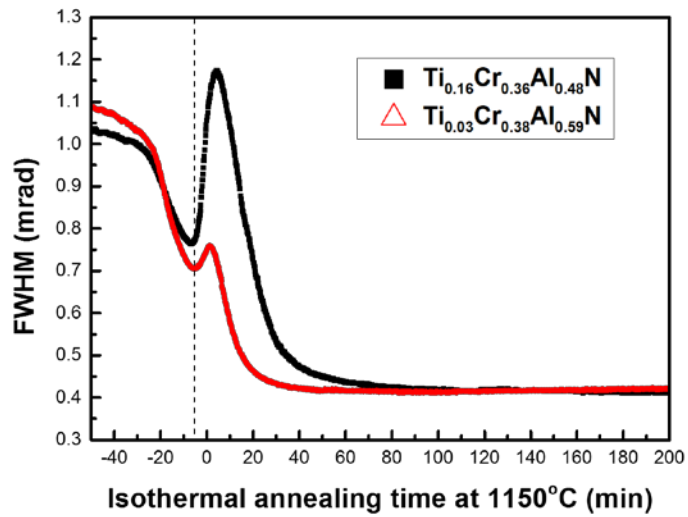


Figure 4 Full-width at half maximum (FWHM) of the c-TiCrAlN 220 diffraction peak as a function of annealing time at 1150 °C.

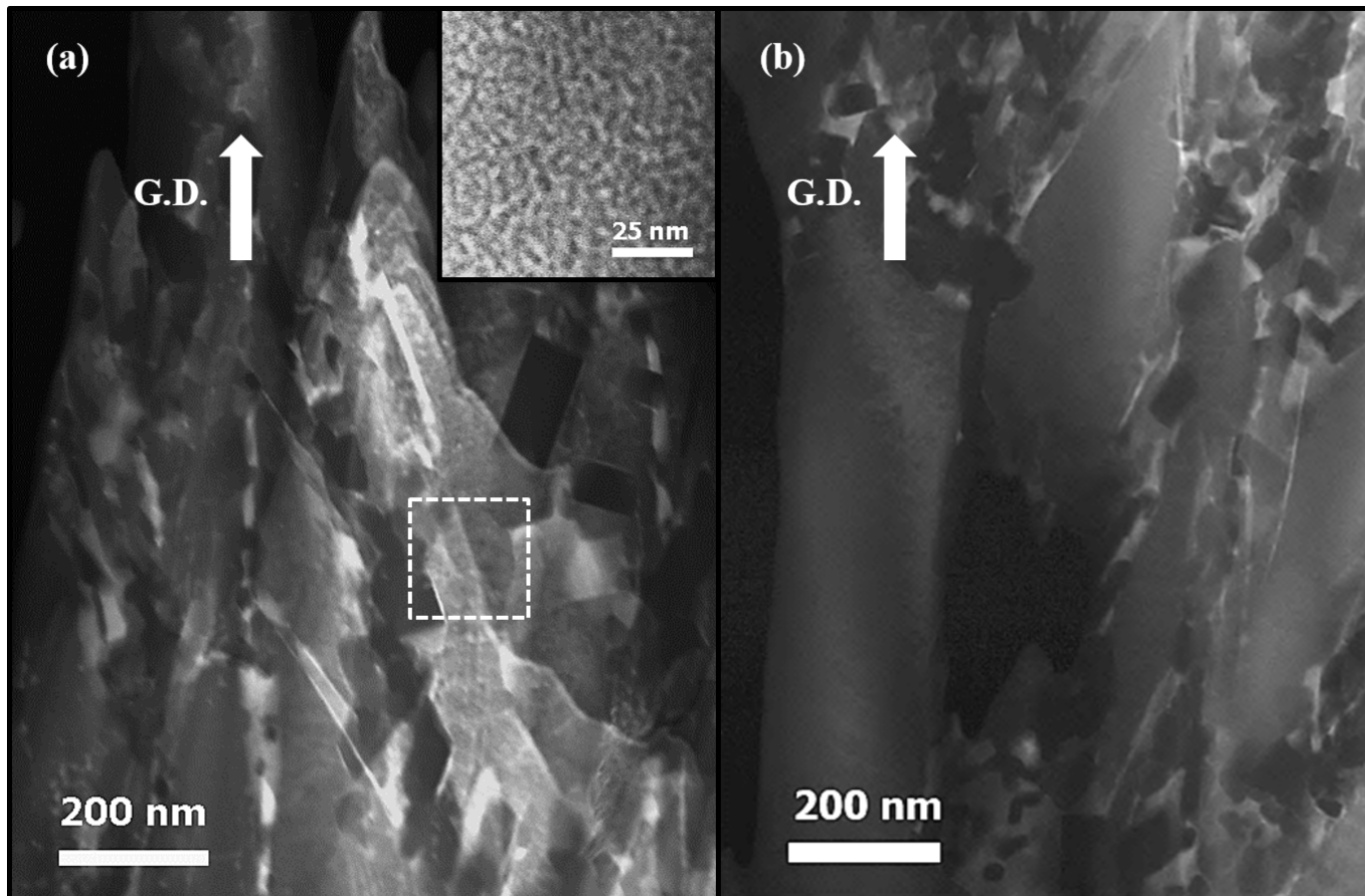


Figure 5 STEM z-contrast micrographs in (a)  $\text{Ti}_{0.16}\text{Cr}_{0.36}\text{Al}_{0.48}\text{N}$  coating annealed at 1150°C for 10 min; (b) the  $\text{Ti}_{0.03}\text{Cr}_{0.38}\text{Al}_{0.59}\text{N}$  coating annealed at 1150°C for 0 min (at the start of isothermal annealing). The inset in (a) is the higher magnification STEM recorded from the marked rectangular region.

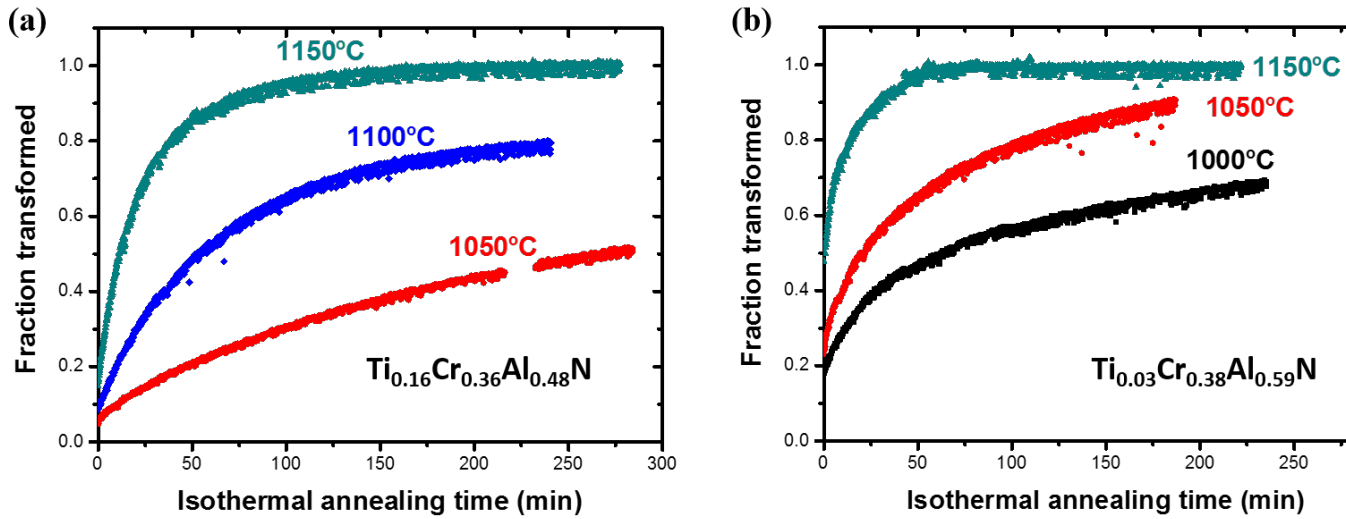


Figure 6 Fraction of transformed h-AlN as a function of isothermal annealing time at different annealing temperatures for (a)  $\text{Ti}_{0.16}\text{Cr}_{0.36}\text{Al}_{0.48}\text{N}$  and (b)  $\text{Ti}_{0.03}\text{Cr}_{0.38}\text{Al}_{0.59}\text{N}$ .

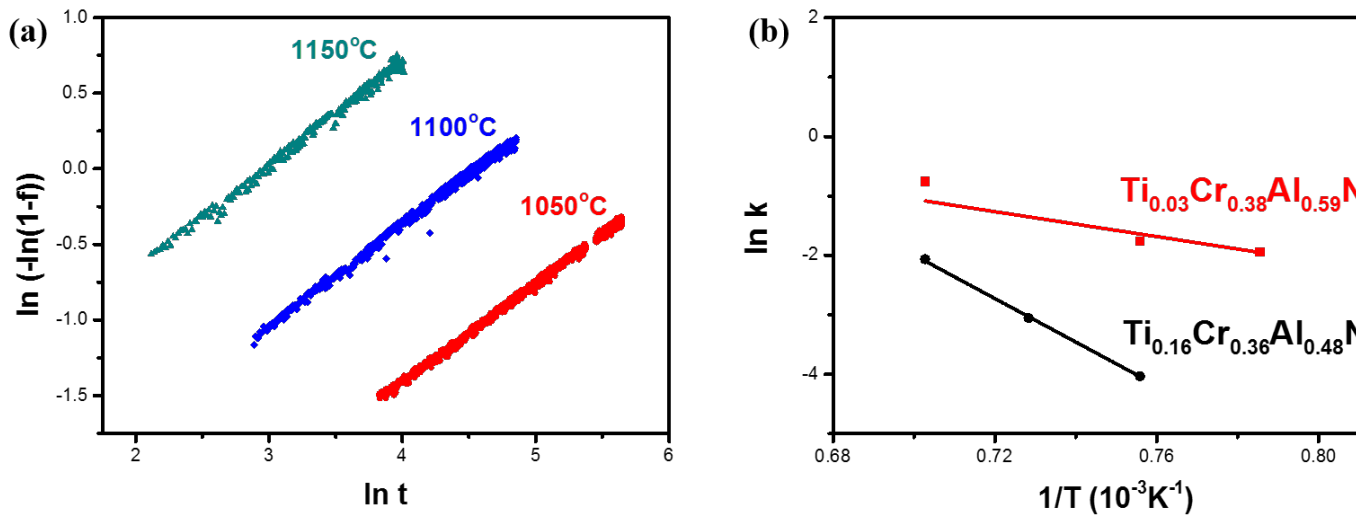


Figure 7 (a) Plot of the experimental data according to Eq. 3 for  $\text{Ti}_{0.16}\text{Cr}_{0.36}\text{Al}_{0.48}\text{N}$  and (b) plot of extracted data from Eq. 3 (symbols) and fitted data (lines) according to Eq. 4 for  $\text{Ti}_{0.16}\text{Cr}_{0.36}\text{Al}_{0.48}\text{N}$  and  $\text{Ti}_{0.03}\text{Cr}_{0.38}\text{Al}_{0.59}\text{N}$ .

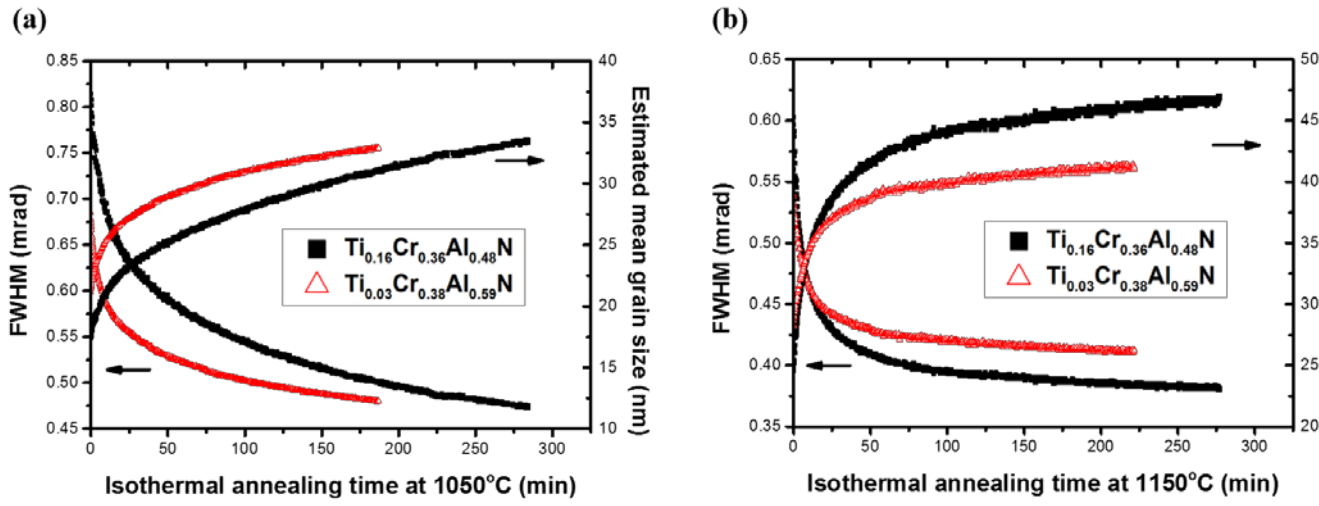


Figure 8 Full-width at half maximum (FWHM) of the h-AlN 100 peak (left axis) and estimated mean h-AlN grain size (right axis) with respect to isothermal annealing time at 1050 °C (a) and 1150 °C (b) in Ti<sub>0.16</sub>Cr<sub>0.36</sub>Al<sub>0.48</sub>N (black) and Ti<sub>0.03</sub>Cr<sub>0.38</sub>Al<sub>0.59</sub>N (red).